Contents lists available at ScienceDirect

Arabian Journal of Chemistry

Original article

Sonochemical synthesis and characterization of holmium stannate nanostructures and their application as photocatalyst for degradation of organic pollutants under simulated sunlight

Makarim A. Mahdi [a], Zeinab Talebzadeh [b], Safaa H. Ganduh [c], Zainab Mohmmad Burhan [a], Layth S. Jasim [a], Masoud Salavati-Niasari [b,*]

[a] Department of Chemistry, College of Education, University of Al-Qadisiyah, Diwaniyah, Iraq
[b] Institute of Nano Science and Nano Technology, University of Kashan, Kashan P. O. Box.87317-51167, Iran
[c] Department of Chemistry Pharmaceutical, College of Pharmacy, University of Al-Qadisiyah, Diwaniyah, Iraq

ARTICLE INFO

ABSTRACT

Manufactured coloring agents are present in our life since they exist in different derivatives varying from furniture to leather accessories to clothes. These toxic combinations are the main components of industrial waste. Diverse techniques have been designed to withdraw organic pollutants from nature. In the present work, an environmentally friendly sonochemical procedure was performed to obtain holmium stannate ($Ho_2Sn_2O_7$) nanoparticles with enhanced photocatalytic performance. The effect of sonication time and power was studied on the structure, morphology, and purity. $Ho_2Sn_2O_7$ were used as a photocatalyst in the UV area due to its suitable bandgap (3.9 eV). The photocatalytic tests indicate that $Ho_2Sn_2O_7$ nanostructures can degrade organic dyes, such as Eriochrome Black T (ECBT), malachite green (MG), and rhodamine B (RhB) in high values. Therefore, the degradation rate is 95.0% under ideal circumstances, which include 100 mg of catalyst and 10 ppm ECBT. According to the kinetics study, the superior rate constant (k = 0.0198 min^{-1}) results in the maximum photocatalytic efficiency (95.0%). Superoxide radicals ($O_2\bullet^-$) and holes (h^+) were found to be the most active radicals implicated in the degradation of ECBT and erythrosine by the scavenger's test.

1. Introduction

Over the past decades, billions of harmful and hazardous contaminants have been discharged into the environment with the fast development of modern industry and agriculture, which remarkably endangers the survival and progress of human beings and the balance of nature (Ali et al., 2020; Arumugam et al., 2021). Among the types of contaminants, organic contaminants in the water and air have provoked widespread concentration since they are potentially carcinogenic and mainly toxic. Organic contaminants in inside/outside air are mostly disgorged from the tex-

tile fabrics, chemical processing industries, indoor furniture coatings, and construction/building materials, etc (Chankhanittha et al., 2020; D. Chen et al., 2020; Kim et al., 2018). Multifarious investigations have demonstrated that organic contaminants in the air are biologically harmful, which can annihilate the ozone layer and boost the formation of photochemical smog, haze, and particulate matter (S. Chen et al., 2020; Mellouki et al., 2015). Also, post-release organic contaminants in the aquatic environment can generate a variety of ecological concerns, even on a small scale, such as negative impacts on aquatic organisms, expanding biochemical oxygen, and clogging of wastewater treatment plants (C.-C. Wang et al., 2014). There are more than 100,000 commercially available dyes with over 7×10^5 tons per year (Chong et al., 2010; C.-C. Wang et al., 2014). These organic dyes are chemically durable and non-biodegradable in water and endanger the environment. Therefore, green approaches for treatment of organic contaminants with high performance and low expense are in critical ultimatum with the increasing concentration on environmental protection and human health. Nowadays, the adsorption procedure and decomposition by photocatalytic reactions are

---

* Corresponding author.
E-mail address: salavati@kashanu.ac.ir (M. Salavati-Niasari).
Peer review under responsibility of King Saud University.

Production and hosting by Elsevier

supposed to be the preceding techniques for terminating organic contaminants from contaminated water and air (Corredor et al., 2021; Gao et al., 2017; Vellingiri et al., 2016). Various research concentrated on the adsorption technique because of its facile operation and simple design (Chen et al., 2010; Vellingiri et al., 2016). Nevertheless, the adsorption method only transmits contaminants from one phase to another phase and reduces their concentration instead of removing them (Yu et al., 2007; Zamora-Ledezma et al., 2021). On the contrary, photocatalysis is a more comprehensive procedure for environmental restoration as it could entirely mineralize organic contaminants into innocuous minerals H_2O and CO_2 under mild circumstances without secondary contamination (Wen et al., 2019).

Additionally, photocatalysis can operate the unlimited sunlight in the photodegradation procedure, preserving a lot of energy (Ahmed et al., 2017). The development of photocatalytic materials is the key to using photocatalytic technology. Nowadays, several photocatalysts have been fabricated and employed for the destruction of organic contaminants in both gaseous and liquid media (Amiri et al., 2017), CdS (Aihemaiti et al., 2021), TiO_2 (Kumar et al., 2022; Li et al., 2022), and ZnO (Aftab et al., 2022; Shkir et al., 2022). When the energy supplied by light radiation is greater than or equal to the bandgap energy of semiconductors, electrons (e^-) in the valence band (VB) are excited to the conduction band (CB), while the holes (h^+) stay in the valence band. Reduction and oxidation half-reactions are then performed with electrons and holes, respectively (Serpone & Emeline, 2012). Nevertheless, these photocatalysts frequently undergo the fast recombination of photoinduced electron-hole (e^--h^+) pairs, leading to inferior photocatalytic performance and insufficient functional applications in the remediation of environmental (Qiu et al., 2018). Hence, investigating new photocatalysts has been drawing tremendous concentration.

Recently, lanthanide-based binary oxides, which crystallize in the pyrochlore structure have acquired a great deal of awareness because of their versatile uses. Their attributes, including ionic conductivity (Sibi et al., 2009), semiconducting behavior (Deepa et al., 2009), ferromagnetism (Knoke et al., 2007), radiation stability (Ewing et al., 2004), luminescence (Zhang et al., 2008), have been investigated in their individual domains of applications. Pyrochlore-type oxides have found their applications as dielectric ceramics for microwave wireless transmission apparatuses, oxygen conductors in fuel cells, anti-reflective/protective coatings, and refractory matrixes for optical instruments, catalysts, nuclear waste-storage materials (Chow et al., 1993) and solid electrolytes (Basu, 2007) in the intermediate temperature solid oxide fuel cells (IT-SOFC). Pyrochlore-based structures of stannates, zirconates, and titanates have been broadly studied with the formation of nuclear waste (de los Reyes et al., 2013; Ewing et al., 2004; Lang et al., 2010). Lanthanide stannate pyrochlores ($Ln_2Sn_2O_7$) reveal much higher variability in response to ion radiation than lanthanide titanate pyrochlores ($Ln_2Ti_2O_7$), which are typically prone to radiation-induced amorphization (Kong et al., 2014). Nevertheless, one of the contributing aspects behind this variation is the problem in assembling high-density lanthanide stannate pyrochlore ceramics.

There are several methods to fabricate nanostructures, including hydrothermal, sol–gel, microwave, sonochemical, co-precipitation, chemical vapor deposition, etc. The sonochemical method, also known as ultrasonic synthesis or ultrasonic-assisted synthesis, offers several advantages over other fabrication methods for the preparation of nanomaterials, including high efficiency, uniform particle size distribution, reduced reaction time, control over particle size and morphology, energy-efficient process, versatility, and scalability (Tian et al., 2020). This study aims to fabricate and characterize the structural pyrochlore $Ho_2Sn_2O_7$ and scrutinizing the photocatalytic activity while keeping the pyrochlore structure. For this purpose, $Ho_2Sn_2O_7$ was fabricated by a facile sonochemical method and the effect of sonication power and time was studied on the morphology, purity, and structure.

2. Material and methods

2.1. Preparation of holmium stannate nanostructures

First, 320 mg of holmium nitrate hexahydrate (0.7 mmol) and 240 mg of tin(IV) chloride pentahydrate (0.68 mmol) were weighed separately and dissolved in a small amount of distilled water. The two solutions were added to each other and mixed. Ammonia was added dropwise to the resulting solution until the pH of the solution reached 11 under ultrasound waves (60 W) for 15 min. The formed colloidal sediments were washed 5 times with distilled water, dried in an oven, and calcined in a furnace

Table 1
Preparation condition of $Ho_2Sn_2O_7$.

Sample No.	Sonication time (min)	Sonication power (W)	Calcination temp. (℃)	Calcination time (h)	Crystal size (nm)	Particle size (nm)
1	15	60	900	5	39.63	45.8
2	10	60			39.57	29.1
3	15	80			39.59	50.6

Scheme 1. Schematic diagram of fabrication process of $Ho_2Sn_2O_7$.

at 900 °C for 5 h. Table 1 and Scheme 1 reveals the different preparation conditions of Ho$_2$Sn$_2$O$_7$ nanostructures.
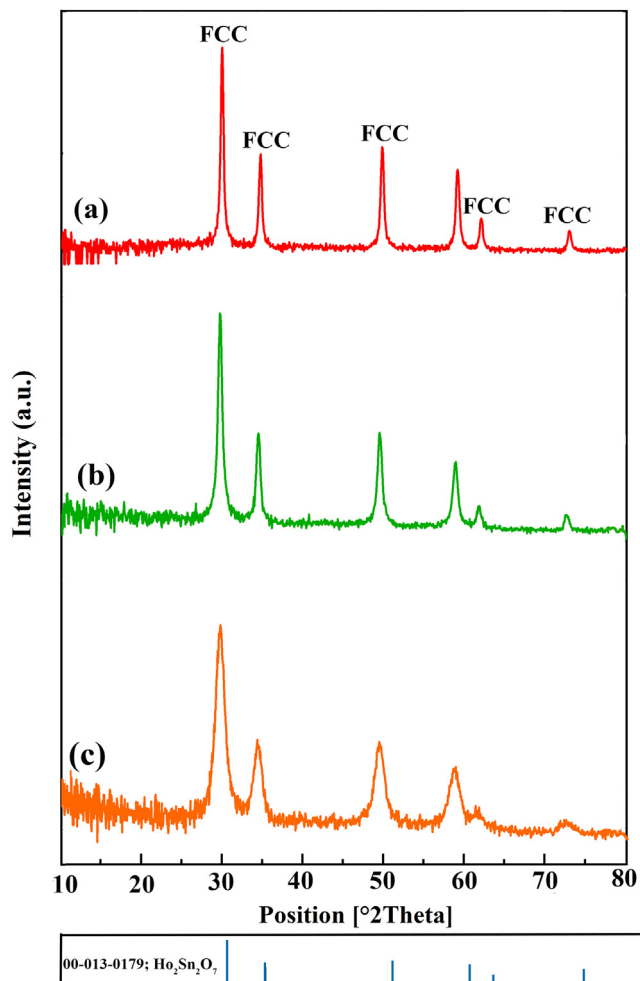

Fig. 1. XRD patterns of Ho$_2$Sn$_2$O$_7$ at different power and time of sonication: (a) 15 min, 60 W, (b)10 min, 60 W, and (c) 15 min, 80 W.

2.2. Photocatalytic procedure
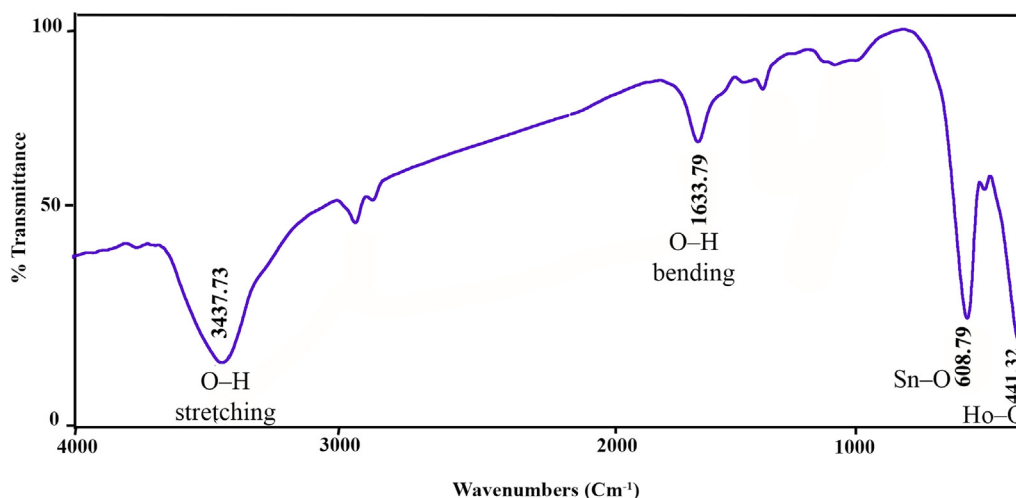
The photocatalytic efficiency of rhodamine B (RhB), eriochrome black T (ECBT), and malachite green (MG) pollutants has been considered to compare the photocatalytic performance of Ho$_2$Sn$_2$O$_7$ nanostructures beneath UV light. 100 mg nanocatalyst was added to 10 ppm organic pollutants (RhB, MG, and ECBT) in each test. The suspension of organic contaminants and catalysts was aerated in the dark for 30 min to achieve the adsorption–desorption balance. The mixture was then exposed to ultraviolet radiation (400 W Osram light). At 20-minute intervals, 2 mL of the solution was removed. After centrifugation, the adsorption of each sample was measured. The destruction efficiency was determined as follow (Monsef & Salavati-Niasari, 2018):

$$\%Destruction\,efficiency = \frac{A_0 - A_t}{A_0} \times 100 \qquad (1)$$

Where A_0 and A_t are the UV–Vis absorption values of the dye solution before and after exposure.

2.3. Physical instruments

XRD patterns were registered to utilize an X-ray diffractogram (Philips) among X' Pert Pro sieved through copper K$_\alpha$ irradiation (λ = 15.4 nm). FT-IR spectra of nanomaterials the samples were recorded by a Shimadzu Varian 4300 spectrophotometer in KBr pellets in the range of 400 to 4000 cm^{-1}. The element examination from the samples was registered using the EDS analysis device with 20 kV stimulating charge. The tiny structure of the outcomes were procured over a MIRA 3 TESCAN field emission scanning electron microscopy. Before catching images, the products were coated by a thin transparent coating of gold to avoid charge accretion and create the product exterior conductive, and achieving a greater dissimilarity. The surface areas (BET) were defined through N$_2$ adsorption at −196 ℃ using an automatic gas adsorption analysis device (Tristar 3000, Micromeritics). Diffuse reflectance UV–vis spectroscopy was performed with a Shimadzu UV/3101 PC ranging from 200 and 800 nm. An MPI Ultrasonic; welding, 1000 W, 20 kHz, Switzerland (multi-wave ultrasound generator) was provided by a transducer/converter. A titanium oscillator was utilized for the ultrasound radiation. Transmission electron microscope (TEM) was carried out employing a TEM Philips EM208 with an accelerating voltage of 100 kV.
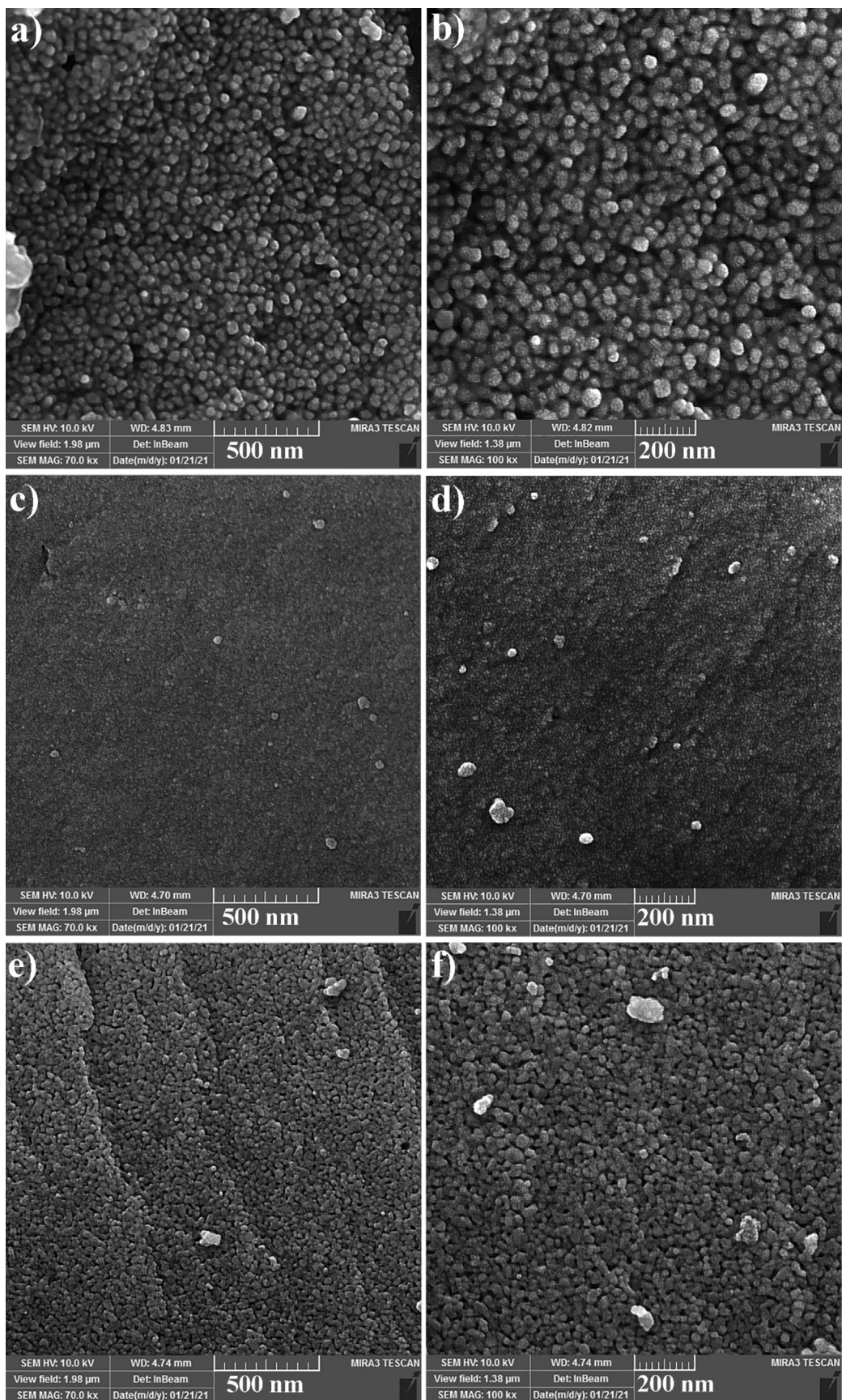

Fig. 2. FTIR spectrum of Ho$_2$Sn$_2$O$_7$ (15 min, 60 W).

Fig. 3. FESEM images of $Ho_2Sn_2O_7$ at different power and time of sonication: (a and b) 15 min, 60 W, (c and d) 10 min, 60 W, and (e and f) 15 min, 80 W.

3. Results and discussion

3.1. Characterization

Fig. 1a demonstrates the XRD pattern of holmium stannate with JCPDS No. 013–0179 having a cubic structure (space group = Fd-3 m) prepared in 15 min and 60 W of sonication. The XRD pattern of $Ho_2Sn_2O_7$ prepared in 10 min and 60 W of sonication is depicted in Fig. 1b, showing all diffraction peaks are matched with $Ho_2Sn_2O_7$ (JCPDS No. 013–0179). Additional remarks on the XRD patterns indicate that both $Ho_2Sn_2O_7$ specimens (Fig. 1a and 1b) have specific intense diffraction peaks, proposing that these nanostructures possess a higher degree of crystallinity. While $Ho_2Sn_2O_7$ prepared in 15 min and 80 W of sonication reveals broader peaks, offering variations in crystallinity and a systematic lattice shift (Fig. 1c). Therefore, the optimum time and power of sonication were chosen to be 15 min and 60 W. The crystallite size of the products was obtained to be about 39 nm (Table 1) utilizing the Scherrer equation (Tahir et al., 2020).

$$D = \frac{0.9\lambda}{\beta \cos\theta} \tag{2}$$

$Ho_2Sn_2O_7$ nanoparticles are generated via ultrasonic radiation. Suitable structures in the nano-scales shape are composed via cavitation produced by ultrasonic waves. According to hot-spot theory, extreme temperatures and tensions are produced with high energies and create active species of radicals (Dheyab et al., 2020). The progress of the fabrication mechanism of the product via the sonochemical approach is displayed below:
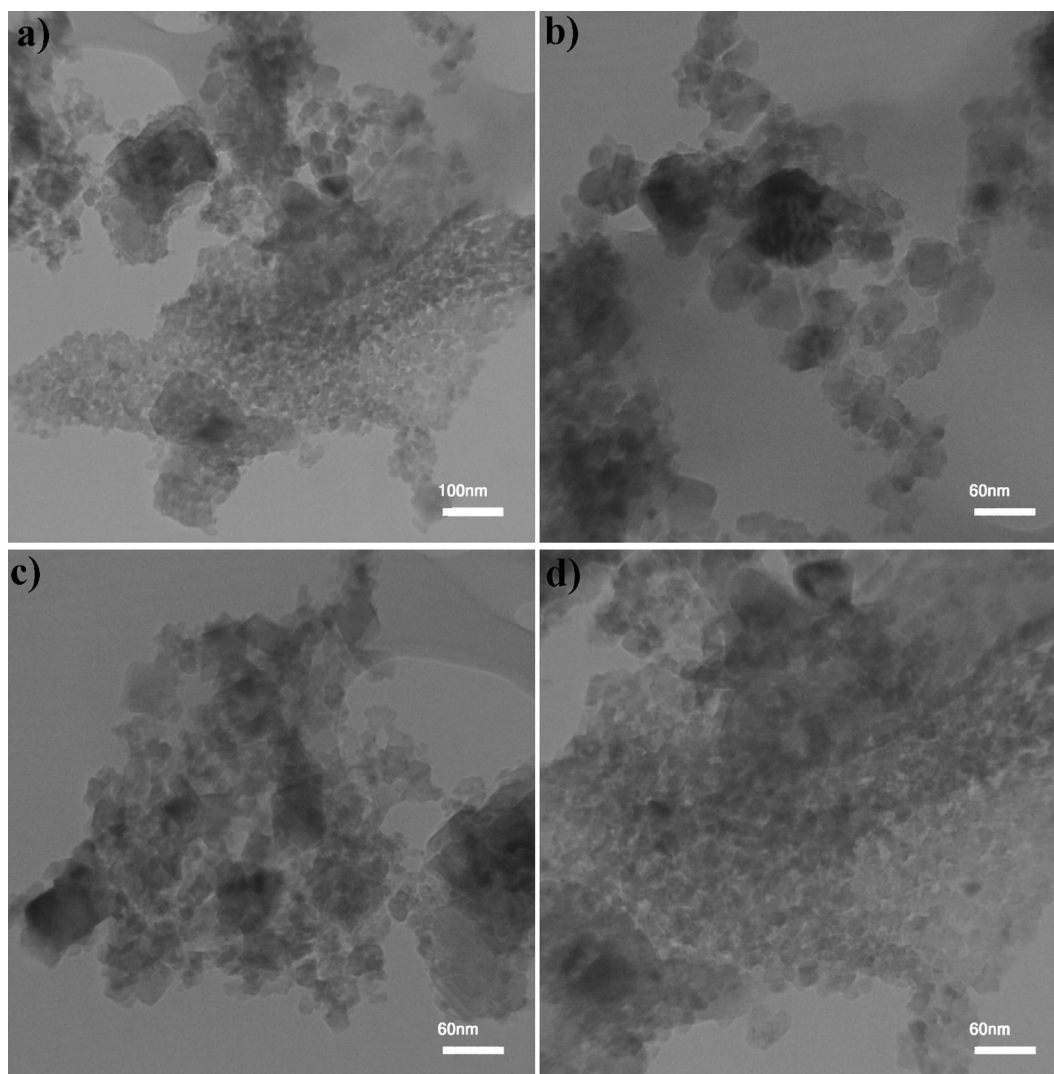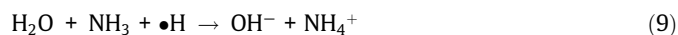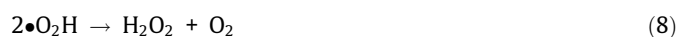
$$H_2O \rightarrow \bullet H + \bullet OH \tag{3}$$

$$\bullet OH + \bullet OH \rightarrow H_2O_2 \tag{4}$$

$$\bullet H + \bullet H \rightarrow H_2 \tag{5}$$

$$\bullet H + O_2 \rightarrow \bullet O_2H \tag{6}$$

$$\bullet H + \bullet O_2H \rightarrow H_2O_2 \tag{7}$$

$$2\bullet O_2H \rightarrow H_2O_2 + O_2 \tag{8}$$

$$H_2O + NH_3 + \bullet H \rightarrow OH^- + NH_4^+ \tag{9}$$

Fig. 4. TEM images of $Ho_2Sn_2O_7$ (15 min, 60 W).

$$Sn^{4+} + OH^- \rightarrow Sn(OH)_4 \qquad (10)$$

$$Ho^{3+} + OH^- + Sn(OH)_4 \rightarrow Ho_2Sn_2O_7 \; nanostructures \qquad (11)$$
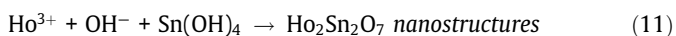
A non-destructive FTIR spectroscopy approach is operated to specify related functional groups in the composition. Depending on the geometrical structure of the adjacent oxygen, in pyrochlore combinations, the metal ions are located in two separate sub-lattices specified as octahedral (N site) and tetrahedral (M site). Pyrochlore oxides have been declared to display seven IR peaks in the wavelength range 500–750 cm^{-1} originating from the bending and vibration of the metal–oxygen (M–O) bonds in the pyrochlore oxide IR spectrum. The peak arrives at around 400 cm^{-1} due to the M–O stretching vibrations in the NO$_6$ octahedron, and the N-O stretching vibrations are located at 600 cm^{-1} (Yang et al., 2011). Fig. 2 illustrates the FT-IR spectrum of Ho$_2$Sn$_2$O$_7$ in
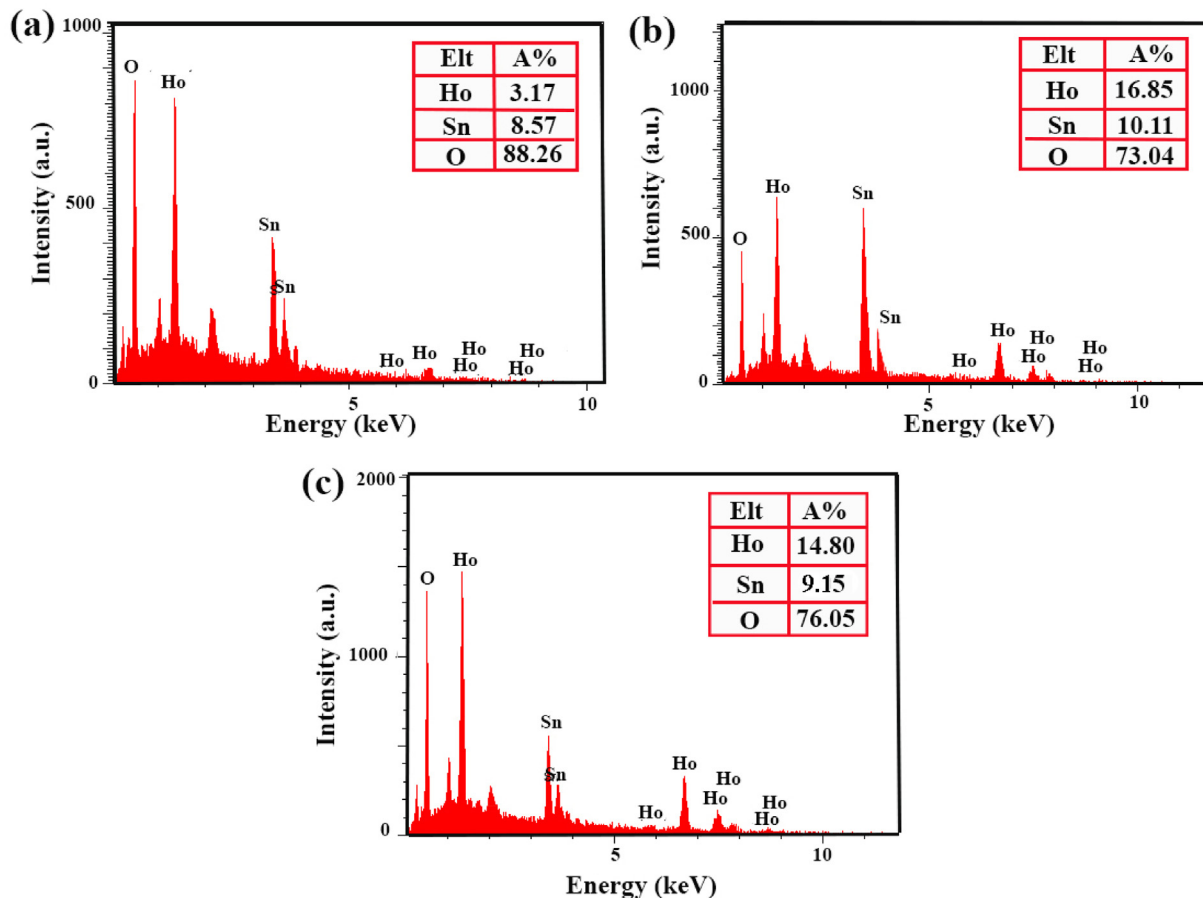

Fig. 5. EDS spectra of Ho$_2$Sn$_2$O$_7$ at different power and time of sonication: (a) 15 min, 60 W, (b)10 min, 60 W, and (c) 15 min, 80 W.
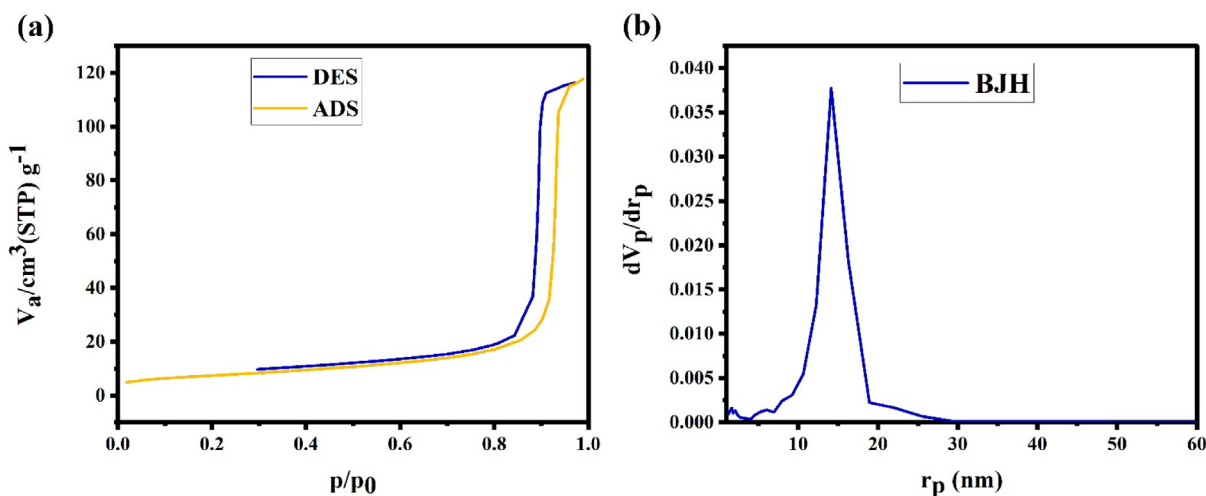

Fig. 6. a) N$_2$ adsorption/desorption isotherm, b) BJH plot of Ho$_2$Sn$_2$O$_7$ (15 min, 60 W).

the wavelength range of 400–4000 cm^{-1}. The absorption bands at 441 cm^{-1} and 608 cm^{-1} elucidated the Ho-O and Sn-O vibrations, respectively. The stretching vibration of OH groups bound to the surface of Sn^{4+} and Ho^{3+} ions is located at 3437 cm^{-1} (Wang et al., 2012). The bending vibration of OH groups is placed at 1633 cm^{-1}.

Fig. 3 unveils the FESEM images of Ho$_2$Sn$_2$O$_7$ nanostructures at different times and powers of sonication. Very uniform nanoparticles with an average diameter of 45.8 nm are composed when the time and power of sonication were 15 min and 60 W (Fig. 3a and 3b). The reduction of time from 15 min to 10 min results in some agglomeration in some areas; however, the medium diameter of particles is 29.1 nm (Fig. 3c and 3d). Increasing the power of sonication from 60 to 80 W causes the particles to stick together and increases the agglomeration (Fig. 3e and 3f). The average particle size in this sample is 50.6 nm. Fig. 4 confirms the average diameter of Ho$_2$Sn$_2$O$_7$ nanoparticles is about 45.0 nm. The homogenous nanoparticles are also observed in Fig. 4.

The EDX result of Ho$_2$Sn$_2$O$_7$ nanoparticles at different times and powers of sonication are displayed in Fig. 5, that the peaks of Ho, Sn, and O confirm the formation of each product purely.

The porosity of Ho$_2$Sn$_2$O$_7$ nanoparticle has been disclosed in Fig. 6. The isotherm category of Ho$_2$Sn$_2$O$_7$ nanoparticles is related to type III and H3-type hysteresis (Fig. 6a). Total pore volume was obtained at 0.182 cm^{3}g^{-1}, average pore diameter was estimated at 27.5 nm, and specific surface (a$_{BET}$) was achieved at 26.47 m^{2}g^{-1}. Fig. 6b manifests the pore size distribution procured from desorption part of the isotherm via the BJH technique. It can be seen that the pore distribution of the generated Ho$_2$Sn$_2$O$_7$ is one-peak.

UV–vis analysis was performed to embody the energy structure of as-prepared samples. The optical attributes of Ho$_2$Sn$_2$O$_7$ nanoparticles are manifested in Fig. 7. The most absorption peaks are in wavelength of 400–650 nm (Fig. 7a), which belong to stannate nanostructures (Dorraji et al., 2017). The optical bandgap energy is determined by the absorbance energy and photon, which was calculated using Tauc method utilizing the following equation:

$$A(h\upsilon - B.G.) = (\alpha h\upsilon)^n \qquad (12)$$

Where υ, α, h, A, and B.G. are the frequency, absorbance, Planck constant, material constant, and optical bandgap, respectively. The energy bandgap of the sample is calculated at 3.9 eV by linear extrapolation of $(\alpha h\upsilon)^2$ versus $h\upsilon$ to zero (Fig. 7b) (Ghanbari & Salavati-Niasari, 2018).
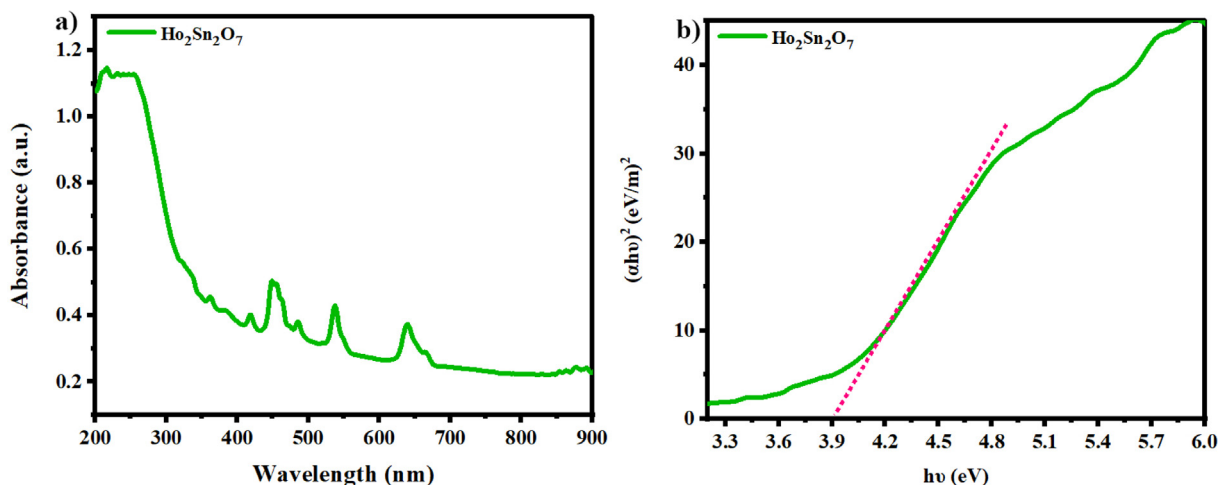
3.2. Photocatalytic behavior and kinetic study

The photocatalytic performance of different dosage of Ho$_2$Sn$_2$O$_7$ NPs was considered over three different organic dyes, including eriochrome black T (ECBT), malachite green (MG), and rhodamine B (RhB). The results of photocatalytic activity are demonstrated in Fig. 8. The photodegradation percentage of ECBT in the presence of 100 mg, 70 mg, and 50 mg of Ho$_2$Sn$_2$O$_7$ is 95%, 70%, and 55%, respectively (Fig. 8a). In addition, the degradation percentage of MG in the presence of 100 mg, 70 mg, and 50 mg of Ho$_2$Sn$_2$O$_7$ are 81%, 71%, and 55%, respectively (Fig. 8c). As observed in Fig. 8e, increasing the Ho$_2$Sn$_2$O$_7$ content also increased the photocatalytic activity of RhB. Increasing the catalyst content increases the surface area available for dye adsorption. This allows more organic dye molecules to come into contact with the catalyst, increasing the chances of a photocatalytic reaction taking place. On the other hand, catalysts provide active sites where chemical reactions can occur. Increasing the catalyst content increases the number of active sites available for dye molecules to interact with, leading to higher photocatalytic activity. Besides, catalysts can absorb light energy and transfer it to the organic dye molecules, promoting their excitation and subsequent reaction. Increasing the catalyst content increases the amount of light absorbed by the system, thereby enhancing its overall photocatalytic activity. Additionally, catalysts facilitate electron transfer between themselves and organic dyes during a photocatalytic reaction. Increasing the catalyst content increases the availability of catalyst particles, allowing for faster and more efficient electron transfer processes, which in turn enhances photocatalytic activity. Overall, increasing the catalyst content in a photocatalytic system provides more opportunities for interaction between organic dyes and catalysts, leading to improved efficiency and higher photocatalytic activity. Table 2 reviews the photocatalytic efficiency of different lanthanide stannate pyrochlores and shows that Ho$_2$Sn$_2$O$_7$ nanostructures can compete well with other lanthanide stannate compounds. Besides, to explore the kinetic impact of samples corresponding to the Langmuir–Hinshelwood system, the values of the remarkable degree of reaction can be developed as follows:

$$\ln\left(\frac{C_0}{C}\right) = kt \qquad (13)$$

Where C$_0$ and Ct are the concentration of pollutant in t = 0 and t min and k is the pseudo-first-order rate constant (min^{-1}). The first-order constant k was obtained from ln(C$_0$/C) linear correlations versus time. The rate constant for Ho$_2$Sn$_2$O$_7$ NPs catalyst is the highest value k = 0.0198 min^{-1} (Fig. 8b, 8d, and 8f).

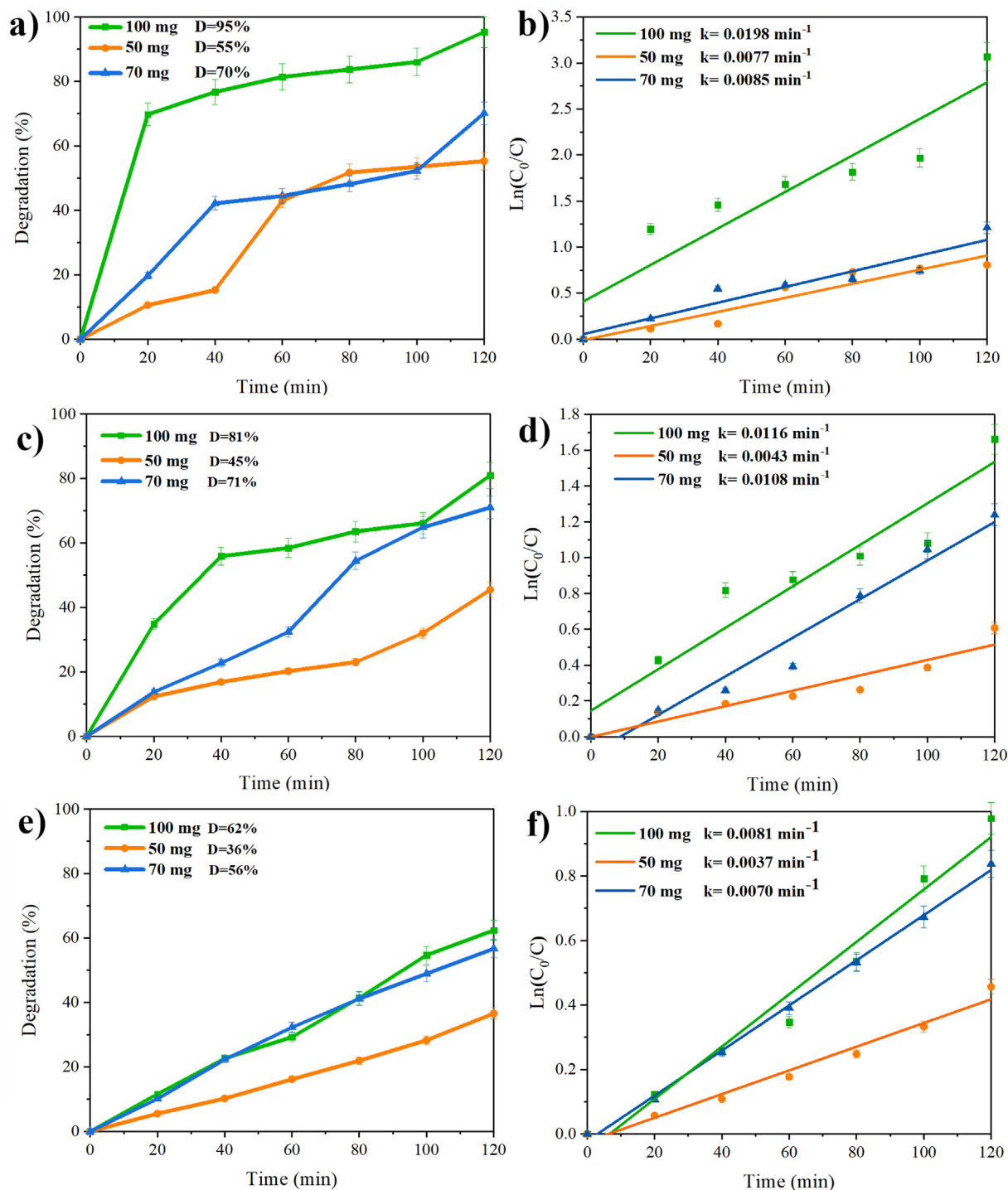**Fig. 7.** a) drs spectrum, b) $(\alpha h\upsilon)^2$ vs. $h\upsilon$ plot of Ho$_2$Sn$_2$O$_7$ (15 min, 60 W).

Fig. 8. Photodegradation of three organic dyes over different $Ho_2Sn_2O_7$ dosages, and Plots of $ln(C_0/C)$ vs time (a and b) ECBT, (c and d) MG, and (e and f) RhB below UV radiation.

Fig. 9 exhibits the effect of scavengers on the photodegradation of ECBT. Three different scavengers, such as EDTA, benzoic acid and benzoquinone were utilized to capture positive holes, hydroxyl radicals, and superoxide radicals, respectively (Sabounchei et al., 2017; Wang et al., 2018; Yin et al., 2020). The degradation efficiency was not reduced in the presence of benzoic acid. An apparent decrease in photocatalytic efficiency was observed by the addition of EDTA and benzoquinone. In short, the effects of different scavengers showed that h⁺ and

$O_2\bullet^-$ recreated influential roles and $\bullet OH$ played an unrelated part in the decolorization of ECBT. Radical formation is largely interrelated in aqueous media, and the radical concentration is influenced by other radicals (Scheme 2). Consequently, the pertinent reactions on the $Ho_2Sn_2O_7$ surface that cause the dye deterioration are depicted below (Dionysiou et al., 2004; Konstantinou & Albanis, 2004):

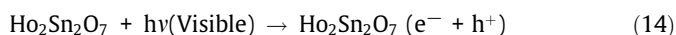$$Ho_2Sn_2O_7 + h\nu(Visible) \rightarrow Ho_2Sn_2O_7 (e^- + h^+) \tag{14}$$

Table 2
Comparison of photocatalytic activity of Lanthanide stannate pyrochlores.

| Catalyst	Synthesis method	Degradation (%)	Dosage	Dye	Light source	Ref.
$Ho_2Sn_2O_7$	Sonochemical	95.0	100 mg	ECBT	UV	This work
$La_2Zr_2O_7$	Sol-gel	57.8	10 mg	Tetracycline	visible	(Wang et al., 2020)
$LaCeZr_2O_7$	Hydrothermal	93.0	–	Indisole Blue	UV	(Gohar et al., 2020)
$La_2Sn_2O_7$	Hydrothermal	95.0	1 g/L	MO	UV	(Zeng et al., 2007)
$Dy_2Sn_2O_7$	Combustion	92.1	76 mg	Acid Violet 7	visible	(Zinatloo-Ajabshir et al., 2020)
$LaDySn_2O_7$	Hydrothermal	94.6	–	direct Indisole blue	UV	(Gohar et al., 2019)
$Yb_2Sn_2O_7$	Hydrothermal	93.0	–	MO	UV	(W. Wang et al., 2014)
$(SrCe)_2Sn_2O_7$	Hydrothermal	51.0	–	4-Nitrophenol	visible	(Jayaraman & Mani, 2019)
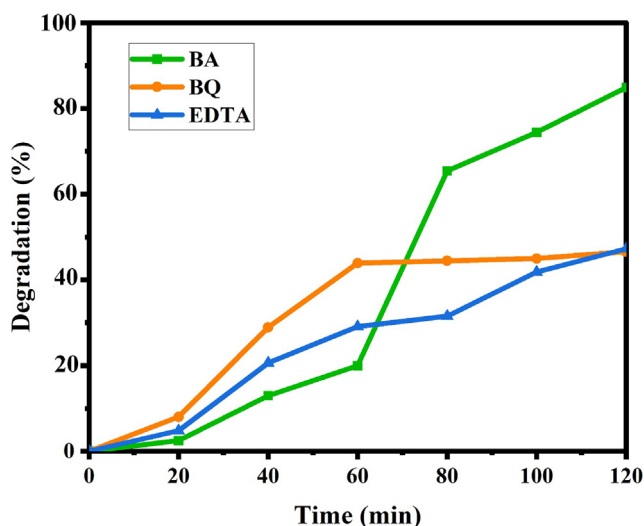
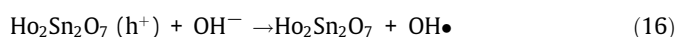**Fig. 9.** Effect of various scavengers.
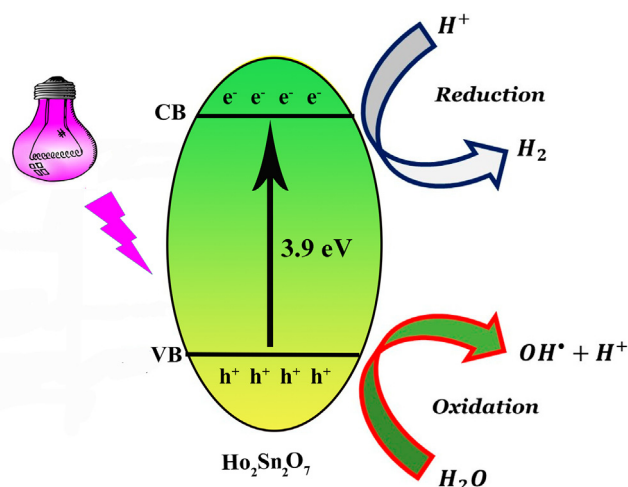
Scheme 2. Schematic diagram of photodegradation of organic pollutants.

$$Ho_2Sn_2O_7 \ (h^+) + H_2O \rightarrow Ho_2Sn_2O_7 + H^+ + OH\bullet \qquad (15)$$

$$Ho_2Sn_2O_7 \ (h^+) + OH^- \rightarrow Ho_2Sn_2O_7 + OH\bullet \qquad (16)$$

$$Ho_2Sn_2O_7 \ (e^-) + O_2 \rightarrow Ho_2Sn_2O_7 + O_2\bullet^- \qquad (17)$$

$$O_2 + e^- \rightarrow O_2\bullet^- \qquad (18)$$

$$H_2O + h^+ \rightarrow \bullet OH + H^+ \qquad (19)$$

$$H^+ + O_2\bullet^- + e^- \rightarrow HOO\bullet \qquad (20)$$

$$H_2O + HOO\bullet \rightarrow \bullet OH + H_2O_2 \qquad (21)$$

$$2H^+ + O_2\bullet^- + e^- \rightarrow H_2O_2 \qquad (22)$$

$$H_2O_2 + e^- \rightarrow OH^- + \bullet OH \qquad (23)$$

$$h^+ + OH^- \rightarrow \bullet OH \qquad (24)$$
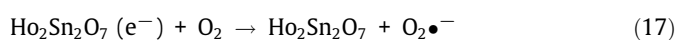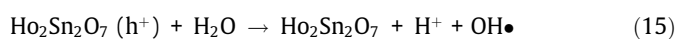
Eriochrome black T + ($O_2\bullet^-$ or h^+ active species) → Degradation products + CO_2 + H_2O (24).

Eriochrome black T + h^+ → ●Eriochrome black T^+ → Degradation products (25).

$O_2\bullet^-$ or h^+ + ●Eriochrome black T^+ → Degradation products (26).

4. Conclusions

Shortly, $Ho_2Sn_2O_7$ nanoparticles were synthesized via a sono-chemical path desiring UV-sensitive catalyst to destroy organic pollutants from water. Effect of nanocatalyst content, dye types, and scavenger kinds was monitored on performance of photocatalytic reaction. According to the DRS data, this compound has an appropriate bandgap (3.9 eV) in UV region. The photocatalytic behavior of $Ho_2Sn_2O_7$ nanoparticles exhibited that this compound has high potential in the destruction of organic dyes, so, 100 mg $Ho_2Sn_2O_7$ can degrade 95.0% of 10 ppm eriochrome black T under UV light. The kinetics study showed that a higher rate constant belongs to the highest photocatalytic performance (k = 0.0198 min^{-1}). Furthermore, three types of scavengers, such as benzoic acid, EDTA, and benzoquinone, were applied to explore the possible mechanism of photodegradation to capture hydroxyl radicals, positive holes, and superoxide radicals, respectively. Finally, superoxide radicals and positive holes were found to support the degradation of ECBT in the UV region.

CRediT authorship contribution statement

Makarim A. Mahdi: Software, Investigation, Methodology. **Zeinab Talebzadeh:** Investigation, Methodology, Formal analysis, Software. **Safaa H. Ganduh:** Writing – review & editing, Data curation. **Zainab Mohmmad Burhan:** Writing – review & editing, Validation. **Layth S. Jasim:** Writing – review & editing, Visualization. **Masoud Salavati-Niasari:** Software, Formal analysis, Methodology, Writing – review & editing, Writing – original draft, Conceptualization, Supervision, Project administration, Investigation, Data curation, Validation, Resources, Visualization, Funding acquisition.

Declaration of Competing Interest

The authors declare that they have no known competing financial interests or personal relationships that could have appeared to influence the work reported in this paper.

Acknowledgment

References

Aftab, S., Shabir, T., Shah, A., Nisar, J., Shah, I., Muhammad, H., Shah, N.S., 2022. Highly efficient visible light active doped ZnO photocatalysts for the treatment of wastewater contaminated with dyes and pathogens of emerging concern. Nanomaterials 12 (3), 486.

Ahmed, M.B., Zhou, J.L., Ngo, H.H., Guo, W., Thomaidis, N.S., Xu, J., 2017. Progress in the biological and chemical treatment technologies for emerging contaminant removal from wastewater: a critical review. J. Hazard. Mater. 323, 274–298.

Aihemaiti, X., Wang, X., Wang, Z., Bai, Y., Qi, K., Ma, Y., Tao, K., Simayi, M., Kuerban, N., 2021. Effective prevention of charge trapping in red phosphorus with nanosized CdS modification for superior photocatalysis. J. Environ. Chem. Eng. 9, (6) 106479.

Ali, N., Said, A., Ali, F., Raziq, F., Ali, Z., Bilal, M., Reinert, L., Begum, T., Iqbal, H.M., 2020. Photocatalytic degradation of congo red dye from aqueous environment using cobalt ferrite nanostructures: development, characterization, and photocatalytic performance. Water Air Soil Pollut. 231 (2), 1–16.

Amiri, M., Salavati-Niasari, M., Akbari, A., Gholami, T., 2017. Removal of malachite green (a toxic dye) from water by cobalt ferrite silica magnetic nanocomposite: herbal and green sol-gel autocombustion synthesis. Int. J. Hydrogen Energy 42 (39), 24846–24860.

Arumugam, M., Lee, S.J., Begildayeva, T., Naik, S.S., Yu, Y., Lee, H., Theerthagiri, J., Choi, M.Y., 2021. Enhanced photocatalytic activity at multidimensional interface of 1D-Bi2S3@ 2D-GO/3D-BiOI ternary nanocomposites for tetracycline degradation under visible-light. J. Hazard. Mater. 404, 123868.

Basu, R.N., 2007. Materials for solid oxide fuel cells. In: Recent Trends in Fuel Cell Science and Technology. Springer, pp. 286–331.

Chankhanittha, T., Somaudon, V., Watcharakitti, J., Piyavarakorn, V., Nanan, S., 2020. Performance of solvothermally grown Bi2MoO6 photocatalyst toward degradation of organic azo dyes and fluoroquinolone antibiotics. Mater. Lett. 258,. https://doi.org/10.1016/j.matlet.2019.126764 126764.

Chen, D., Cheng, Y., Zhou, N., Chen, P., Wang, Y., Li, K., Huo, S., Cheng, P., Peng, P., Zhang, R., 2020. Photocatalytic degradation of organic pollutants using TiO2-based photocatalysts: A review. J. Clean. Prod. 268, 121725.

Chen, S., Huang, D., Zeng, G., Xue, W., Lei, L., Xu, P., Deng, R., Li, J., Cheng, M., 2020. In-situ synthesis of facet-dependent BiVO4/Ag3PO4/PANI photocatalyst with enhanced visible-light-induced photocatalytic degradation performance: Synergism of interfacial coupling and hole-transfer. Chem. Eng. J. 382, 122840.

Chen, C., Ma, W., Zhao, J., 2010. Semiconductor-mediated photodegradation of pollutants under visible-light irradiation. Chem. Soc. Rev. 39 (11), 4206–4219.

Chong, M.N., Jin, B., Chow, C.W., Saint, C., 2010. Recent developments in photocatalytic water treatment technology: a review. Water Res. 44 (10), 2997–3027.

Chow, R., Falabella, S., Loomis, G.E., Rainer, F., Stolz, C.J., Kozlowski, M.R., 1993. Reactive evaporation of low-defect density hafnia. Appl. Opt. 32 (28), 5567–5574.

Corredor, J., Rivero, M.J., Ortiz, I., 2021. New insights in the performance and reuse of rGO/TiO2 composites for the photocatalytic hydrogen production. Int. J. Hydrogen Energy 46 (33), 17500–17506.

de los Reyes, M., Whittle, K. R., Zhang, Z., Ashbrook, S. E., Mitchell, M. R., Jang, L.-Y., & Lumpkin, G. R. (2013). The pyrochlore to defect fluorite phase transition in Y 2 Sn 2− x Zr x O 7. RSC advances, 3(15), 5090-5099.

Deepa, K., Rao, P.P., Radhakrishnan, A., Sibi, K., Koshy, P., 2009. Pyrochlore type semiconducting ceramic oxides in Ca–Ce–Ti–M–O system (M= Nb or Ta)—Structure, microstructure and electrical properties. Mater. Res. Bull. 44 (7), 1481–1488.

Dheyab, M., Aziz, A.A., Jameel, M.S., Khaniabadi, P.M., Mehrdel, B., 2020. Mechanisms of effective gold shell on Fe3O4 core nanoparticles formation using sonochemistry method. Ultrason. Sonochem. 64, 104865.

Dionysiou, D.D., Suidan, M.T., Baudin, I., Laîné, J.-M., 2004. Effect of hydrogen peroxide on the destruction of organic contaminants-synergism and inhibition in a continuous-mode photocatalytic reactor. Appl. Catal. B: Environ. 50 (4), 259–269.

Dorraji, M.S., Amani-Ghadim, A., Rasoulifard, M., Taherkhani, S., Daneshvar, H., 2017. The role of carbon nanotube in zinc stannate photocatalytic performance improvement: experimental and kinetic evidences. Appl. Catal. B: Environ. 205, 559–568.

Ewing, R.C., Weber, W.J., Lian, J., 2004. Nuclear waste disposal—pyrochlore (A 2 B 2 O 7): Nuclear waste form for the immobilization of plutonium and "minor" actinides. J. Appl. Phys. 95 (11), 5949–5971.

Gao, Y., Li, S., Li, Y., Yao, L., Zhang, H., 2017. Accelerated photocatalytic degradation of organic pollutant over metal-organic framework MIL-53 (Fe) under visible LED light mediated by persulfate. Appl. Catal. B: Environ. 202, 165–174.

Ghanbari, M., Salavati-Niasari, M., 2018. Tl4CdI6 nanostructures: facile sonochemical synthesis and photocatalytic activity for removal of organic dyes. Inorg. Chem. 57 (18), 11443–11455.

Gohar, R.S., Karamat, N., Mumtaz, S., Ahmad, B., Shah, A., Ashiq, M.N., 2019. Facile synthesis of LaDySn2O7 SnSe nanocomposite with excellent photocatalytic Activity under visible light. Mater. Chem. Phys. 229, 362–371.

Gohar, R.S., Ehsan, M.F., Karamat, N., Najam-Ul-Haq, M., Shah, A., Nisar, J., Qureshi, A.M., Ashiq, M.N., 2020. Photomineralization of untreated wastewater by a novel LaCeZr2O7–SnSe nanocomposite as a visible light driven heterogeneous photocatalyst. Solid State Sci. 106, 106305.

Jayaraman, V., Mani, A., 2019. Optical, photocatalytic properties of novel pyro-stannate A2Sn2O7 (A= Ce, Ca, Sr), and Pt deposited (SrCe) 2Sn2O7 for the removal of organic pollutants under direct solar light irradiation. Mater. Sci. Semicond. Process. 104, 104647.

Kim, B., Lee, Y.-R., Kim, H.-Y., Ahn, W.-S., 2018. Adsorption of volatile organic compounds over MIL-125-NH2. Polyhedron 154, 343–349.

Knoke, G., Niazi, A., Hill, J., & Johnston, D. (2007). Synthesis, structure, and ferromagnetism of the oxygen defect pyrochlore system Lu 2 V 2 O 7− x (x= 0.40–0.65). Physical Review B, 76(5), 054439.

Kong, L., Zhang, Y., Karatchevtseva, I., Blackford, M.G., Lumpkin, G.R., Triani, G., 2014. Synthesis and characterization of Nd2SnxZr2− xO7 pyrochlore ceramics. Ceram. Int. 40 (1), 651–657.

Konstantinou, I.K., Albanis, T.A., 2004. TiO2-assisted photocatalytic degradation of azo dyes in aqueous solution: kinetic and mechanistic investigations: a review. Appl. Catal. B: Environ. 49 (1), 1–14.

Kumar, A., Choudhary, P., Kumar, A., Camargo, P.H., Krishnan, V., 2022. Recent advances in plasmonic photocatalysis based on TiO2 and noble metal nanoparticles for energy conversion, environmental remediation, and organic synthesis. Small 18 (1), 2101638.

Lang, M., Zhang, F., Zhang, J., Wang, J., Lian, J., Weber, W.J., Schuster, B., Trautmann, C., Neumann, R., Ewing, R.C., 2010. Review of A2B2O7 pyrochlore response to irradiation and pressure. Nucl. Instrum. Methods Phys. Res., Sect. B 268 (19), 2951–2959.

Li, Z., Wang, S., Wu, J., Zhou, W., 2022. Recent progress in defective TiO2 photocatalysts for energy and environmental applications. Renew. Sustain. Energy Rev. 156, 111980.

Mellouki, A., Wallington, T., Chen, J., 2015. Atmospheric chemistry of oxygenated volatile organic compounds: impacts on air quality and climate. Chem. Rev. 115 (10), 3984–4014.

Monsef, R., Ghiyasiyan-Arani, M., Salavati-Niasari, M., 2018. Application of ultrasound-aided method for the synthesis of NdVO4 nano-photocatalyst and investigation of eliminate dye in contaminant water. Ultrason. Sonochem. 42, 201–211.

Qiu, J., Zhang, X., Feng, Y., Zhang, X., Wang, H., Yao, J., 2018. Modified metal-organic frameworks as photocatalysts. Appl. Catal. B: Environ. 231, 317–342.

Sabounchei, S.J., Hosseinzadeh, M., Zarepour-jevinani, M., Ghanbari, B., 2017. Monodentate palladium(0)–[60]fullerene complexes of diphosphine ligands as efficient and sustainable nanocatalysts for the Mizoroki-Heck coupling reaction of aryl chlorides [10.1039/C7NJ00741H]. New J. Chem. 41 (18), 9701–9709. https://doi.org/10.1039/C7NJ00741H.

Serpone, N., & Emeline, A. (2012). Semiconductor Photocatalysis☐ Past, Present, and Future Outlook. In (Vol. 3, pp. 673-677): ACS Publications.

Shkir, M., Palanivel, B., Khan, A., Kumar, M., Chang, J.-H., Mani, A., AlFaify, S., 2022. Enhanced photocatalytic activities of facile auto-combustion synthesized ZnO nanoparticles for wastewater treatment: An impact of Ni doping. Chemosphere 291, 132687.

Sibi, K., Radhakrishnan, A., Deepa, M., Rao, P.P., Koshy, P., 2009. Oxide ion conductivity and relaxation in CaREZrNbO7 (RE= La, Nd, Sm, Gd, and Y) system. Solid State Ion. 180 (20–22), 1164–1172.

Tahir, M.B., Nawaz, T., Nabi, G., Sagir, M., Rafique, M., Ahmed, A., Muhammad, S., 2020. Photocatalytic degradation and hydrogen evolution using bismuth tungstate based nanocomposites under visible light irradiation. Int. J. Hydrogen Energy 45 (43), 22833–22847.

Tian, X.-X., Gholamrezaei, S., Amiri, O., Ghanbari, M., Dashtbozorg, A., Salavati-Niasari, M., 2020. Zn2MnO4/ZnO nanocomposites: One step sonochemical fabrication and demonstration as a novel catalyst in water splitting reaction. Ceram. Int. 46 (16), 25789–25801.

Vellingiri, K., Kumar, P., Kim, K.-H., 2016. Coordination polymers: Challenges and future scenarios for capture and degradation of volatile organic compounds. Nano Res. 9 (11), 3181–3208.

Wang, C., Huang, W., Wang, Y., Cheng, Y., Zou, B., Fan, X., Yang, J., Cao, X., 2012. Synthesis of monodispersed La2Ce2O7 nanocrystals via hydrothermal method: a study of crystal growth and sintering behavior. Int. J. Refract Metal Hard Mater. 31, 242–246.

Wang, Y.-C., Lee, A.-H., Chen, C.-C., 2018. Perovskite-like photocatalyst, PbBiO2Br/PbO/g-C3N4: Synthesis, characterization, and visible-light-driven photocatalytic activity. J. Taiwan Inst. Chem. Eng. 93, 315–328.

Wang, C.-C., Li, J.-R., Lv, X.-L., Zhang, Y.-Q., Guo, G., 2014. Photocatalytic organic pollutants degradation in metal–organic frameworks. Energ. Environ. Sci. 7 (9), 2831–2867.

Wang, W., Liang, S., Bi, J., Jimmy, C.Y., Wong, P.K., Wu, L., 2014. Lanthanide stannate pyrochlores Ln2Sn2O7 (Ln= Nd, Sm, Eu, Gd, Er, Yb) nanocrystals: synthesis, characterization, and photocatalytic properties. Mater. Res. Bull. 56, 86–91.

Wang, Z., Wang, Y., Huang, L., Liu, X., Han, Y., Wang, L., 2020. La2Zr2O7/rGO synthesized by one-step sol-gel method for photocatalytic degradation of tetracycline under visible-light. Chem. Eng. J. 384, 123380.

Wen, M., Li, G., Liu, H., Chen, J., An, T., Yamashita, H., 2019. Metal–organic framework-based nanomaterials for adsorption and photocatalytic degradation

of gaseous pollutants: recent progress and challenges. Environ. Sci. Nano 6 (4), 1006–1025.

Yang, J.-Y., Su, Y.-C., Liu, X.-Y., 2011. Hydrothermal synthesis, characterization and optical properties of La2Sn2O7: Eu3+ micro-octahedra. Trans. Nonferrous Met. Soc. Chin. 21 (3), 535–543.

Yin, X.-T., Li, J., Dastan, D., Zhou, W.-D., Garmestani, H., Alamgir, F.M., 2020. Ultra-high selectivity of H2 over CO with a pn nanojunction based gas sensors and its mechanism. Sens. Actuators B: Chem. 319, 128330.

Yu, H., Zhang, K., Rossi, C., 2007. Theoretical study on photocatalytic oxidation of VOCs using nano-TiO2 photocatalyst. J. Photochem. Photobiol. A Chem. 188 (1), 65–73.

Zamora-Ledezma, C., Negrete-Bolagay, D., Figueroa, F., Zamora-Ledezma, E., Ni, M., Alexis, F., Guerrero, V.H., 2021. Heavy metal water pollution: A fresh look about hazards, novel and conventional remediation methods. Environ. Technol. Innov. 22, 101504.

Zeng, J., Wang, H., Zhang, Y., Zhu, M.K., Yan, H., 2007. Hydrothermal synthesis and photocatalytic properties of pyrochlore La2Sn2O7 nanocubes. J. Phys. Chem. C 111 (32), 11879–11887.

Zhang, A., Lü, M., Yang, Z., Zhou, G., Zhou, Y., 2008. Systematic research on RE2Zr2O7 (RE= La, Nd, Eu and Y) nanocrystals: Preparation, structure and photoluminescence characterization. Solid State Sci. 10 (1), 74–81.

Zinatloo-Ajabshir, S., Morassaei, M.S., Amiri, O., Salavati-Niasari, M., 2020. Green synthesis of dysprosium stannate nanoparticles using Ficus carica extract as photocatalyst for the degradation of organic pollutants under visible irradiation. Ceram. Int. 46 (5), 6095–6107.